

Adsorption of Congo red azo dye on nanosized SnO₂ derived from sol-gel method

Elaziouti Abdelkader^{1,2} · Laouedj Nadjia^{1,2} · Vannier Rose-Noëlle³

Received: 7 April 2015 / Accepted: 7 October 2015 / Published online: 12 November 2015
© The Author(s) 2015. This article is published with open access at Springerlink.com

Abstract The nanoparticles tin oxide (SnO₂) has been successfully synthesized via a sol-gel method. The as-prepared SnO₂ was characterized using thermogravimetric analysis coupled with mass spectroscopy, X-ray diffraction and scanning electron microscope. Batch experiments were carried out to study the adsorption kinetics of Congo red azo dye on SnO₂. The effect of varying parameters such as contact time, initial dye concentration and adsorbent dose on the adsorption process was investigated. The results showed that the SnO₂ catalysts has high crystallinity with tetragonal rutile structure and average particle size about 13–23 nm. The untreated sample SnO₂-80 exhibited high efficiency (84.41 %) after 60 min of exposure time, which was 2 times as much as that of SnO₂-450 sample. The adsorption process was found to be highly dye concentration and adsorbent dose dependent. Pseudo-second-order kinetic model gave the best fit, with highest correlation coefficients ($R^2 \geq 0.99$). Regarding the adsorption equilibrium, the experimental results suggest that the Langmuir

model was applicable. The formation of hydrogen bond and the electrostatic interaction between the Sn²⁺ center and the electron rich nitrogen atoms of CR moiety were believed to be the main adsorption mechanism. These findings should be valuable for designing effectively adsorbent material and practical interest in terms of ecology and sustainable development.

Keywords Sol-gel method · SnO₂ · Congo red · Adsorption activity

Introduction

Tin oxide (SnO₂) has been attracting a great deal of research interest owing to its outstanding physical and chemical properties. Investigation has shown that SnO₂ has a high exciton binding energy of 130 meV [1], high chemical stability and excellent resistivity variation in a gaseous atmosphere. These intriguing properties make SnO₂ a promising candidate for basic research and technological applications alike. Tin oxide is a versatile wide band gap (3.6 eV at 300 K) [2], n-type semiconducting oxide with an extensive potential of applications including solid-state gas sensors [3], dye-based solar cells [4], field emission displays [5], luminescent devices [6]. This oxide is among the few with the band gap energy near to visible light [7, 8]. In the last decade, SnO₂ has been studied as promising material with many unique surface properties including luminescence and photocatalytic activity [8, 9]. Adsorption is a conventional but efficient technique to remove heavy metals or organics from aqueous solutions. Adsorption techniques for wastewater treatment have become more popular in recent years owing to their efficiency in the removal of pollutants too stable for biological

✉ Elaziouti Abdelkader
elaziouti_a@yahoo.com

Laouedj Nadjia
nlaouedj@yahoo.fr

Vannier Rose-Noëlle
rose-noelle.vannier@ensc-lille.fr

¹ Laboratory of Inorganic Materials Chemistry and Application, Department of Physical Chemistry, University of the Science and the Technology of Oran (USTO M.B), El M'naouar, BP 1505, 31000 Oran, Algeria

² Dr. Moulay Tahar University, Saida, Algeria

³ Unit of Catalysis and Solid State Chemistry of Lille University Cité Scientifique, Bâtiment C7 Avenue Mendeleïev, Villeneuve d'Ascq, B.P. 90108, 59652 Lille, France

methods. Recently, enormous efforts have been directed toward the development of size-controlled synthesis of various functional materials in current applications such as microemulsion [4], hydrothermal [10], gel combustion [11], sol-gel and ultrafiltration [12], thermal decomposition [13] and surfactant-assisted solvothermal method [14]. Sol-gel method is one of the most widely used techniques to produce SnO₂ powders and factors, such as pH medium, initial concentration, calcinations temperature, and aging time are important to the process [15–17].

Sol-gel method is an outstanding route to the synthesis of hybrid nanoparticles and nanocomposites. Generally speaking it gives inorganic high purity materials at mild synthesis conditions (temperature and pH). An outstanding variation is the so-called Stober method allowing colloidal particles (with well-defined size and shape and with narrow size distribution) be produced through hydrolysis and polycondensation of silicon alkoxides in water/alcohol/ammonia mixtures. The sol-gel method allows, also, easy functionalization of silica nanoparticles with specific organic groups. Many of the hybrid nanoparticles synthesis methods take advantage of all this. The sol-gel method finds, however, applications in many other research fields [18].

In the present study, nanostructured tin oxide (SnO₂) was synthesized via a sol-gel method. The as-prepared SnO₂ samples were characterized using thermogravimetric analysis coupled with mass spectroscopy (TG-SM), X-ray diffraction (XRD) and scanning electron microscope (SEM). Batch experiments were carried out to study the adsorption kinetics of Congo red azo dye, as probe pollutant, on SnO₂. The effect of varying parameters such as contact time, initial dye concentration and adsorbent dose on the adsorption process was investigated. Experimental kinetic data were tested with the pseudo-first-order and pseudo-second-order kinetic equations.

Experimental

Materials

The starting materials were tin dichloride dihydrate (SnCl₂·2H₂O; 98 wt%) and oxalic acid dihydrate (H₂C₂O₄; 99.5 wt.%) and SnO₂ (99.99 wt.%) were all obtained from Aldrich chemical company ltd. Congo red (C.I. 22020, MW = 696.67 g mol⁻¹, C₃₂H₂₄N₆O₆S₂·2Na, λ_{max} = 497 nm and pKa = 4; 99.99 wt%) and other chemicals used in the experiments (NH₄OH and H₂SO₄) were purchased from C.I.S.A Espagne. Distilled water was used for preparation of various solutions. The Congo red dye structure and its characteristics are given in Table 1.

Preparation of ultrafine n-SnO₂

SnO₂ was synthesized using co-precipitation method. In a typical synthesis procedure, tin dichloride dehydrate, SnCl₂·2H₂O, was dissolved in 250 ml of deionized water to reach a Sn(II) concentration of 0.4 M. The obtained white turbid suspension was magnetically stirred for 1 h at room temperature. A stoichiometric amount of oxalic acid, which was used as the chelating agent to complex the cations, then were added dropwise to the aqueous solution of tin dichloride in the molar ratio 1:1 with respect to the cations (Sn). The resulting suspension was kept under stirring for a further 4 h and the precipitate was finally collected by centrifugation, washed with deionized water and ethanol for 3 times in order to remove the excess retained chloride ions. Complete removal of the chloride ions was confirmed with the silver nitrate test applied to the supernatant. The precipitate was washed twice with ethanol to reduce agglomeration by interparticle bridging [19]. The washed precipitate was then dried at 80 °C for 24 h (denoted as SnO₂-80) after which it was ground with an agate mortar. The as-synthesized nanostructured SnO₂ were heated in temperature range from 450 to 650 °C for 4 h, respectively. The SnO₂ samples after annealing (denoted as SnO₂-450 and SnO₂-650, respectively). The commercial SnO₂ sample (denoted as SnO₂-com). A schematic illustration of the synthesis method was depicted in Fig. 1.

Characterization

The crystalline structure of the catalysts were characterized by powder X-ray diffraction (XRD) employing a scanning rate of 10°/min in a 2θ range from 10° to 70°, in a Bruker D8 Advance diffractometer using monochromatized CuKα radiation (λ = 1.5406 Å). The crystalline average size (d_{DRX}) was assessed using calculation using the Debye–Scherrer equation [20–22] equation as follows Eq. (1):

$$d_{\text{DRX}} = \frac{0.9\lambda}{\beta \sin \theta} \quad (1)$$

where $\beta = \sqrt{(\text{FWHM})^2 - (0.3)^2}$ and λ is the X-ray wavelength (1.5406 Å). FWHM is the full-width at half maximum and θ is the Bragg angle. FWHM was calculated from the peak having highest intensity in all the samples. The lattice constants of the samples calculated from their corresponding XRD pattern data are obtained by full proof of program. The crystallite sizes of the pure nanoparticles were deduced from the XRD patterns by calculation of the Scherrer equation.

The morphologies of the samples were observed by scanning electron microscopy (SEM), which were taken on a S4800 Field Emission SEM (FESEM, Hitachi, Japan),

Table 1 The molecular structure and chemical properties of Congo red dye (CR)

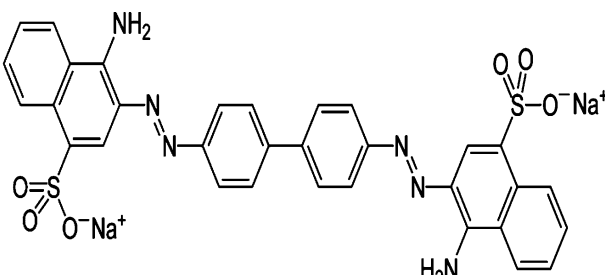
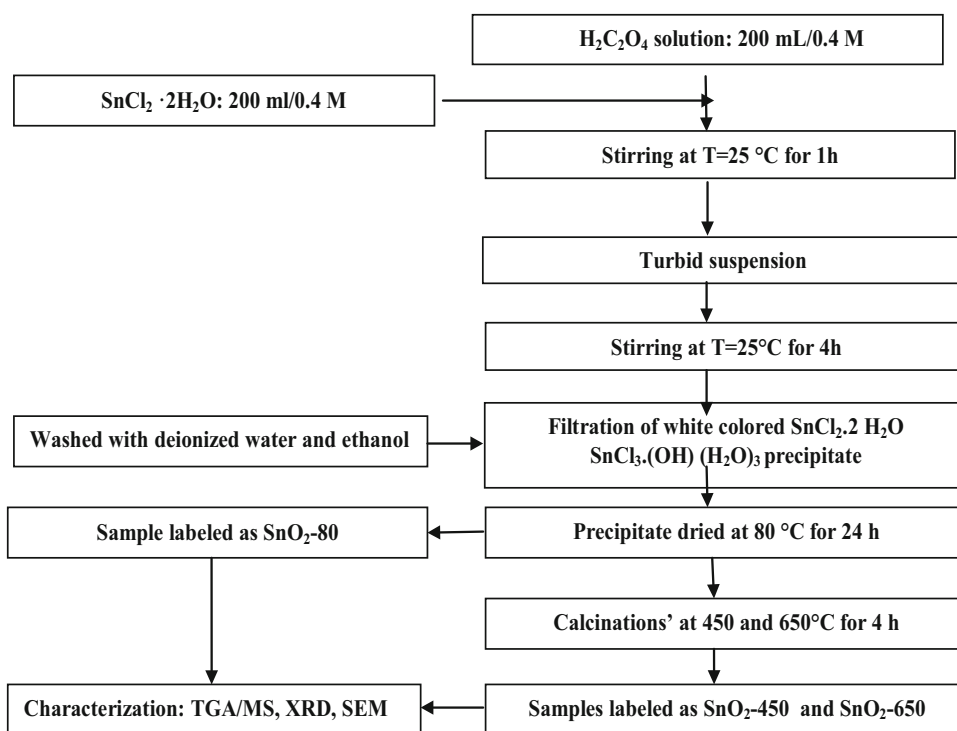
Molecular structure	Chemicals properties	
	Chemical formula	C ₃₂ H ₂₂ N ₆ Na ₂ O ₆ S ₂
	λ max (nm)	497
	Chemical class	Diazo dye
	Mw (g/mol)	696.665
	C.I. number	22120
	pKa	4

Fig. 1 Schematic illustration of the synthesis of nanostructured SnO₂ by a chemical precipitation process

using an accelerating voltage of 15 kV. Thermogravimetric analysis coupled with mass (TG-SM) was performed with a Setaram Instrument, at heating rate of 10 °C/min, a temperature range from 25 to 800 °C, in air gas purge of 30 ml/min with a sample weight of 22.4 mg.

Sorption study

Adsorption kinetics experiments were carried out as a single-stage batch test using a magnetically stirrer at 298 K using 250 mL beaker containing 100 mL different concentrations of dye solutions and doses of sorbent. The initial pH of dye

solutions was adjusted at 7 by HCl and NaOH solutions using digital pH-meter using HANNA HI 83141. At given intervals, 5 mL aliquots were collected, centrifuged using EBA-Hetlich centrifuge at 3500 rpm for 15 min, and then filtered to remove the catalyst particles for analysis. The filtrates were finally monitored using a UV–Vis spectrophotometer using (UV–Vis Spectrometer Shimadzu UV mini-1240), in the λ range from 200 to 800 nm, using 1 cm optical pathway cells and computing from the calibration curves. The experiments were done by varying the contact time (0–60 min), concentration of dye solution (20–50 mg/L) and amount of adsorbent (0.375–1 g/L).



Isotherm studies

Adsorption experiments were carried out as a single-stage batch test using a magnetically stirrer. A suspension containing 0.1 g of adsorbent sample was mixed with a 100 mL aqueous solution of dye at a known initial concentration and initial pH in a flask. The initial pH values of the solutions were previously adjusted to 7. Aliquots of the solution were withdrawn at predetermined time intervals and were centrifuged at 3500 rpm for 15 min to remove any adsorbent particles. Dye concentrations in the supernatant solutions were subsequently estimated by measuring absorbance at maximum wavelength of dye by spectrophotometer. The adsorption tests were continued until the equilibrium concentration was reached. The adsorption capacity of CR dye was researched over a range of concentration from 10 to 50 mg/L.

The adsorption capacity Q (mg/g) was calculated based on a mass balance equation as given below Eq. (2):

$$Q(\text{mg/g}) = \left[\frac{(C_e - C_t)}{m} \right] v \quad (2)$$

The removal efficiency is expressed as follows Eq. (3):

$$\eta(\%) = \left[\frac{(C_i - C_f)}{C_i} \right] \times 100 \quad (3)$$

where Q is the adsorption capacity of the adsorbate (mg/g), m is the weight of adsorbent (g), v is the volume of solution (L), and C_o (mg/L) and C_e (mg/L) are initial and equilibrium concentration of adsorbate in solution, respectively.

Results and discussions

TG-MS analysis

TGA was used to clarify the appropriate heat treatment temperature for the tin complex. Coupling a mass spectrometer (MS) to a thermogravimetric analysis (TG) allows evolved gases to be analyzed and identified giving this additional valuable information. Figure 2, shows TG-SM curves of the SnO₂-80 sample heated up to $T = 800$ °C. The TG curve shows three well defined regions of weight loss. The first mass loss involved the dehydration of two H₂O molecules and the formation of insoluble SnC₂O₄ crystals occurs during the heating from 25 °C to $T = 80$ °C. Tin oxalate (SnC₂O₄) is stable until 250 °C and will be transformed completely into SnO₂ at 330 °C as shown in the region of second mass loss. In this step, the organic ligand and other residues were continuously oxidized by heating from 250° to 330 °C. The second sequential weight loss displayed an even rapid and was

found to be 50 %. Hardly any further weight loss in the TG curve can be observed at temperatures above 330 °C, indicating the completion of reaction as shown in the third sequential weight loss. The dehydration of hydroxide precursor and removal of organics in the form of oxides of carbon, the most likely dioxide of carbon by heating from $T = 270$ to $T = 450$ °C which was characterized at the MS curves by the highest intense peak at $T = 380$ °C and the lowest intense peak at $T = 350$ °C, respectively. As shown in Fig. 2, the chemical reaction finishes at about 380 °C, resulting in the formation of SnO₂ powder [13]. Based on the thermal analysis results mentioned above, $T = 450$ °C was selected as appropriate calcination temperature for the precursors.

XRD analysis

The XRD patterns of the nanostructured SnO₂ are shown in Figs. 3 and 4. Diffraction peaks SnO₂-80 sample (Fig. 3) was indexed as the pure monoclinic structure of tin oxalate (SnC₂O₄) lattice constant $a = 10.3708$ Å et $b = 5.5035$ Å and $c = 8.7829$ Å (which is in good agreement with standard value (JCPDS file No. 22-496). Diffraction peaks of SnO₂-com (Fig. 4a) at 2θ of 26.63°, 33.73°, 37.94°, and 51.79° can be indexed as the (110), (101), (200), and (211) planes of tetragonal rutile-like SnO₂ [Cassiterite, Joint Committee on Powder Diffraction Standards (JCPDS) card No. 41-1445, space group: $P42/mnm$, lattice constant $a = 4.7373(2)$ Å et $b = 3.1865(3)$ Å]. The relative intensities of (101) and (110) peaks are the largest. No characteristic peaks of impurities were observed, indicating the high purity of the product. The SnO₂-450 and (Fig. 4c) and SnO₂-650 (Fig. 4b) samples were also perfectly indexed as the pure tetragonal rutile structure of stannic oxide. The low index (110) face is the thermodynamically most-stable bulk termination in oxides and has the lowest surface energy [14]. It means that SnO₂ prefer to grow along the [110] direction, forming the SnO₂ nanostructure. The lattice constant of nanoparticle samples calculated from their corresponding XRD pattern data are obtained by full proof program were found to be $a = 4.743(2)$ Å and $b = 3.189(2)$ Å for SnO₂-450 sample, $a = 4.758(2)$ Å and $b = 3.1875(8)$ Å for SnO₂-650 sample. Here, we observe that the XRD patterns in the 2θ range from 20° to 41° (Fig. 5) show that the SnO₂-450 and SnO₂-650 samples exhibit broadened peaks with a little shift toward lower intensities. Based on the Scherrer equation, the crystallite size of a sample is inversely proportional to the full-width-half-maximum (FWHM), indicating that a broader peak represents smaller crystallite size [23]. Thus, the higher temperature promotes the crystallinity and a consequent broadening of the diffraction peaks of the as-synthesized nanoparticles. The highest broadening of the diffraction

Fig. 2 Thermogravimetric analysis (TGA) coupled with mass spectroscopy (MS) of the SnO₂-80 precursor nanostructures

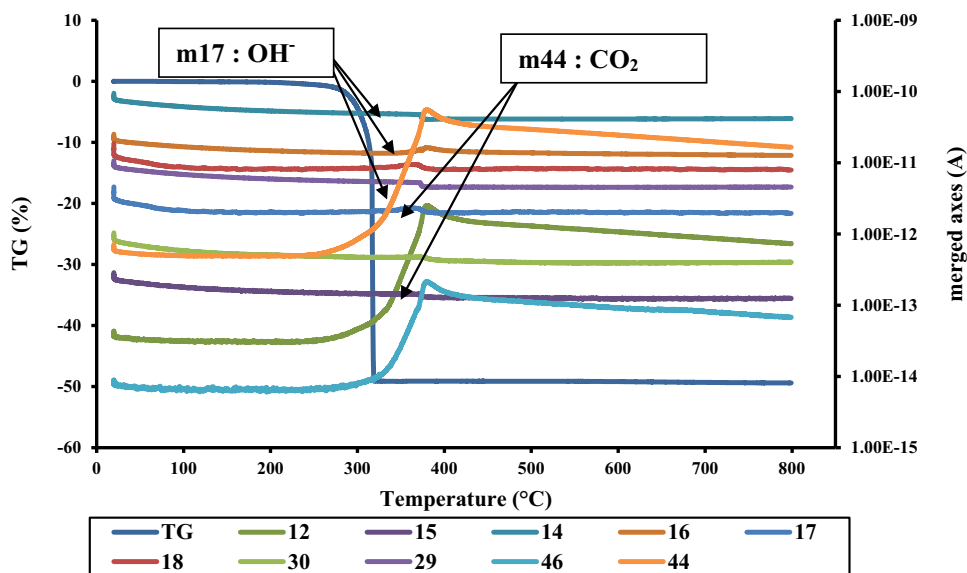
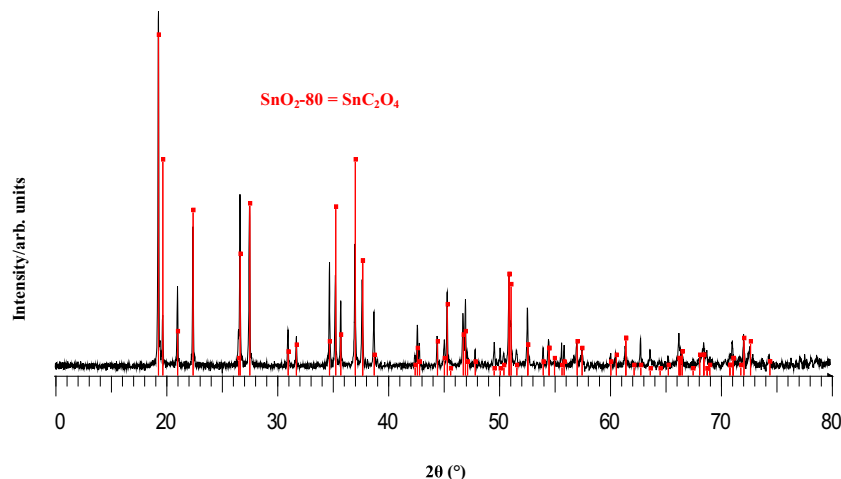


Fig. 3 XRD pattern of tin oxalate SnC₂O₄ (denoted as SnO₂-80) nanoparticles



peaks is observed for SnO₂-450 sample. The crystallite sizes of SnO₂-com, SnO₂-450 and SnO₂-650 samples deduced from the XRD patterns by calculation of the Scherrer equation showed that crystalline size, d_{XRD} were found to be 50, 13 and 23 nm, respectively. The crystallographic parameters obtained on the SnO₂ nanostructure powders given in Table 2 show that the calcination temperature did significantly decrease the crystallite size (increase the surface area) of the material SnO₂. At 80 and 450 °C, an increase in the calcination temperature caused a remarkable decline of the crystallite size, which was not the case at 650 °C where the relatively higher calcination temperature significantly improved the crystallite size from 13 to 23 nm, this can be explained by the fact that at the thermal activation at 650 °C, the material particles became so finer, reducing the porosity of the surface and hence compacting it to generate a lower surface area. A previous

study of [24] reported on the synthesis of the submicron tin oxide (SnO₂) from tin(II) chloride and oxalic acid in air. It was found that the spherical particles of a very consistent diameter of 75 nm. For the SnO₂ sample synthesized via the modified polyacrylamide gel route, in a recent published study [25] reported a calculated crystallite size of the sample prepared by using oxalic acid as the chelating agent at 118 nm. Another study on the synthesis of the nanoparticles tin oxide (SnO₂) using citric acid as the chelating agent at 15 nm [26]. Therefore, our values are much lower than the reported data.

SEM analysis

Figure 6, illustrates typical SEM images of the as-synthesized tin oxides compared to SnO₂-com samples. The SnO₂-com morphologies consisted of large spherical

Fig. 4 XRD patterns of SnO₂-com (a), SnO₂-450 (b) and SnO₂-650 (c) nanoparticles

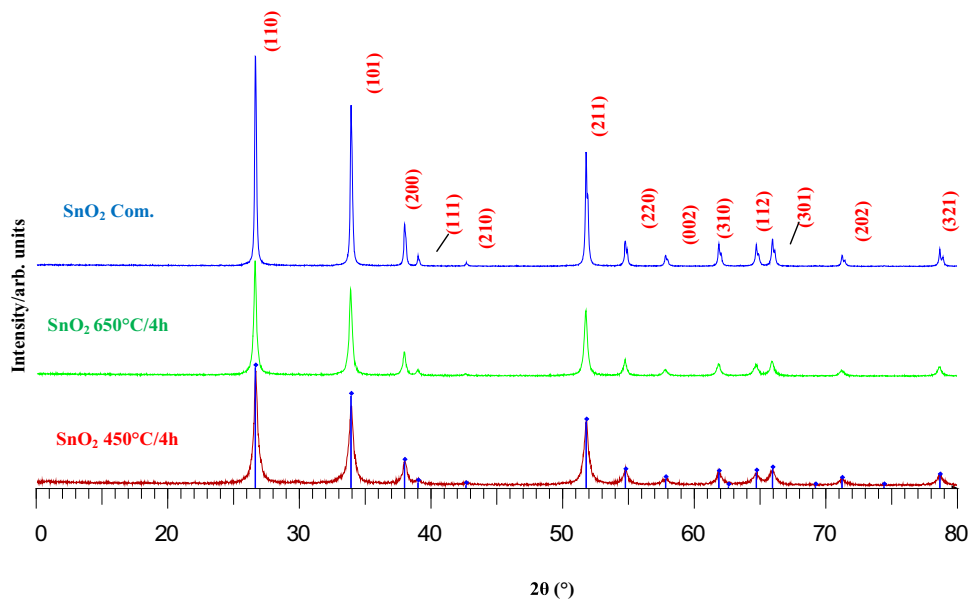


Fig. 5 XRD patterns of SnO₂-com (blue color), SnO₂-450 (red color) and SnO₂-650 (green color) nanoparticles in the 2θ range from 20° to 41°

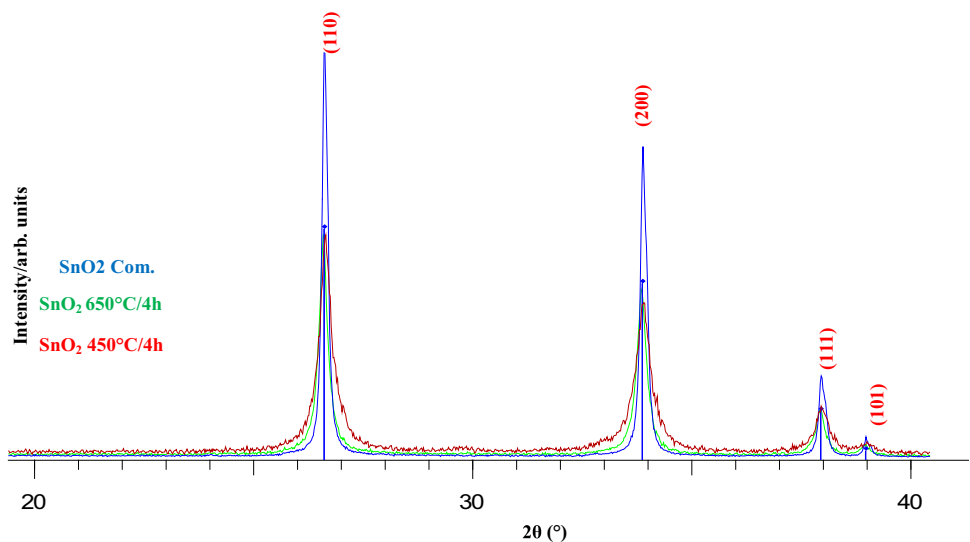


Table 2 Crystallographic parameters of the as-synthesized SnO₂ nanoparticles

Samples	Crystal structure	Unit cell parameter 'a' and 'b' (Å)	Crystallite size (nm)
SnO ₂ (JCPDS No. 41-1445)	Tetragonal	$a = 4.7373$ (2); $c = 3.1865$ (3)	–
SnO ₂ -com	Tetragonal	$a = 3.1875$ (8); $c = 4.738$ (2)	50
SnO ₂ -80 (SnC ₂ O ₄)	Monoclinic	$a = 10.3708$; $b = 5.5035$; $c = 8.7829$	–
SnO ₂ -450	Tetragonal	$a = 4.743$ (2); $c = 3.189$ (2)	13
SnO ₂ -650	Tetragonal	$a = 4.738$ (2); $c = 3.1875$ (8)	23

aggregates of smaller individual nanostructures, as shown in Fig. 6a. Figure 6b illustrates typical high-resolution SEM image of SnO₂-com sample to further show the details of the nanostructure. As seen in Fig. 6b, it clearly SEM analysis (Fig. 6b) shows two different spherical-

shaped nanostructures on the SnO₂ surfaces, which can be assigned to SnO₂ with a particle size in the range of 0.1 μm and SnO with approximately 0.2 μm dimensions. Compared to SnO₂-com, the morphology of SnO₂-80 (Fig. 6c) consisted of mixtures of individual and

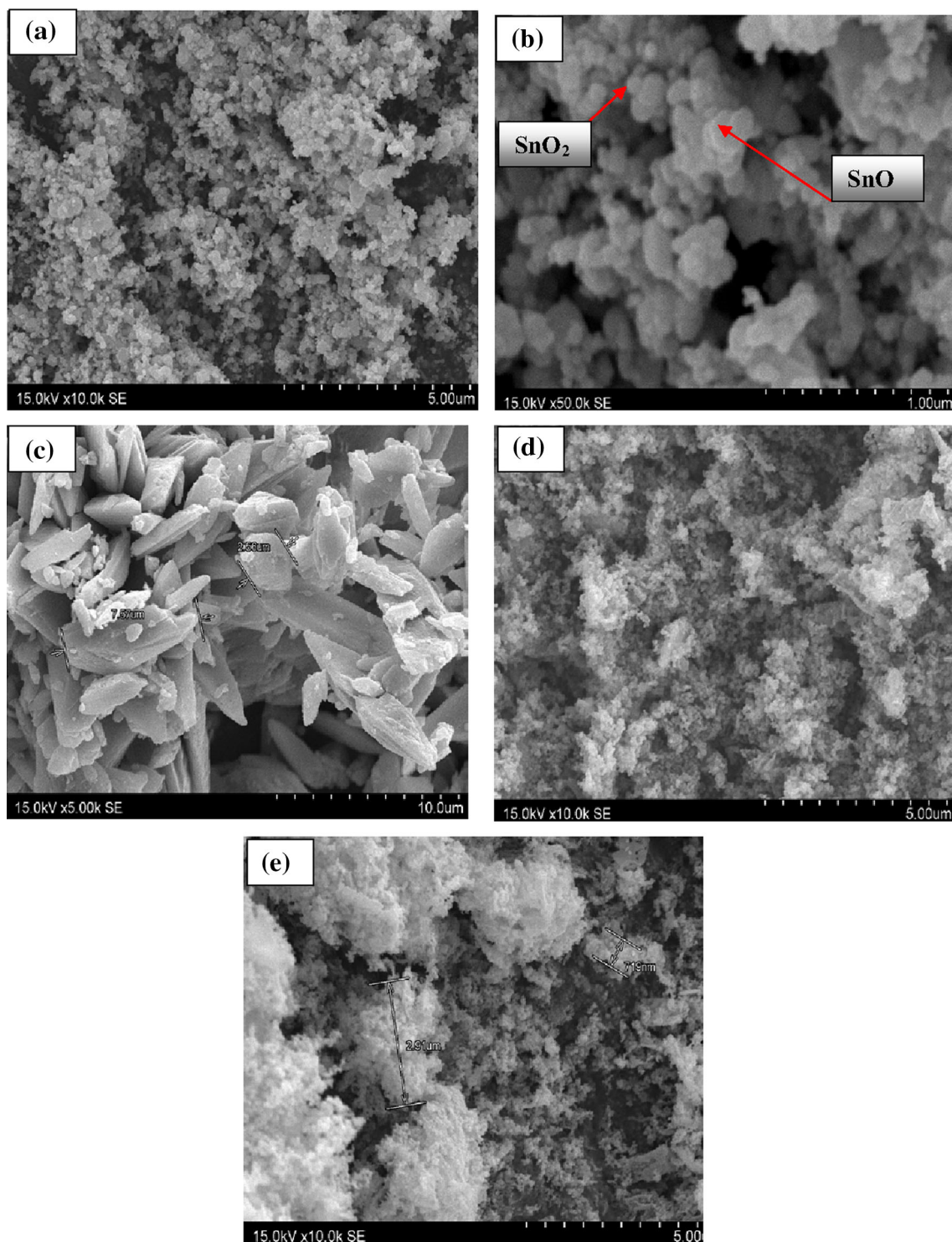


Fig. 6 SEM images of SnO_2 : **a** low-resolution of SnO_2 -com, **b** high-resolution of SnO_2 -com, **c** SnO_2 -80 (SnC_2O_4), **d** SnO_2 -450 and **e** SnO_2 -650 nanoparticles

intergrowths of elongated prisms, with a particle size in the range of 3–10 μm . Figure 6d, e, display the SEM images of SnO_2 -450 and SnO_2 -650 samples, revealing that the nanostructures consisted of a foamed body, which

resulted from the gas release during decomposition. Previous published study [27] reported on the oxidation of VOC_2O_4 to V_2O_3 . It was suggested that the reaction gases form a shell around the oxide particles during calcination,

which can limit agglomeration. As the calcinations temperatures were increased up to 450 °C, the aggregation of the particles becomes more dominant. This can be attributed to the higher solubility and collision between particles. A strong degree of the foamed nanostructures with size about 750–3 μm was observed in SnO₂-650 sample, which agrees with the XRD results. The different morphology reveals the key role of individual the oxalate acid chelating agent in controlling the nucleation and crystal orientation.

Removal properties of CR

Effect of contact time

Figure 7 illustrates the effect of time on the removal of Congo red (CR) dye on SnO₂-80, SnO₂-450 and SnO₂-com samples. The adsorption of this dye is fast in the first 10–30 min, and then gradually slows until equilibrium is reached. The equilibrium time obtained is basically depends on the nature of the explored material. As displayed in Table 3, the sorption efficiency of CR over the SnO₂-80 nanoparticles was more than 84.41 % after 60 min of contact time, which was approximately 2 times as much as that of SnO₂-450 (50.05 %) and was slight equal to SnO₂-com (83.33 %). The obviously enhanced sorption efficiency of SnO₂-80 catalyst was primarily caused by the balance of the high crystallinity and the large surface area for adsorbing substrates, in agreement with XRD and SEM results. However, these requirements are in general conflict with each other, because the crystallinity increases with the heat treatment temperature, while the surface area decreases. These data indicated that the

Table 3 Adsorption efficiency for CR adsorption of SnO₂-80, SnO₂-450 and SnO₂-com nanoparticles samples [(CR) = 20 mg/L, (m/v) = 0.5 g/L, pH 7, T = 298 K and contact time of 60 min]

Materials	Adsorption efficiency η (%)
SnO ₂ -80	84.41
SnO ₂ -450	51.05
SnO ₂ -com	83.33

removal of CR was not related to the available surface area; the SnO₂-80 nanoparticles exhibited a lower surface area, but it had higher adsorption efficiency.

This highlights that the adsorption of anionic dye, although believed to be primary an electrostatic interaction between the Sn²⁺ center and the electron rich nitrogen atoms of CR moiety, is rather complicated by many factors other than the surface characteristics of the adsorbent, such as dye–dye interaction.

For the SnO₂-450 sample, the thermal activation at 450 °C, the material particles became so finer (high structure crystallinity), reducing the porosity of the surface and hence compacting it to generate a lower surface area for absorbing substrates, and therefore decreasing the number of active sites and the attraction between the dye and the SnO₂-450 surface [28]. Hence the sequential sorption activity was as follow:

$$\eta_{\text{CR/SnO}_2-80} > \eta_{\text{CR/SnO}_2-\text{com}} > \eta_{\text{CR/SnO}_2-450}$$

Effects of initial dye concentration

The effects of initial dye concentration as a function of contact time were conducted in the range of 0–60 min. The

Fig. 7 Adsorption kinetic for CR adsorption on SnO₂-80, SnO₂-450 and SnO₂-com nanoparticles samples [(CR) = 20 mg/L, (m/v) = 0.5 g/L, pH 7, T = 298 K and contact time of 60 min]

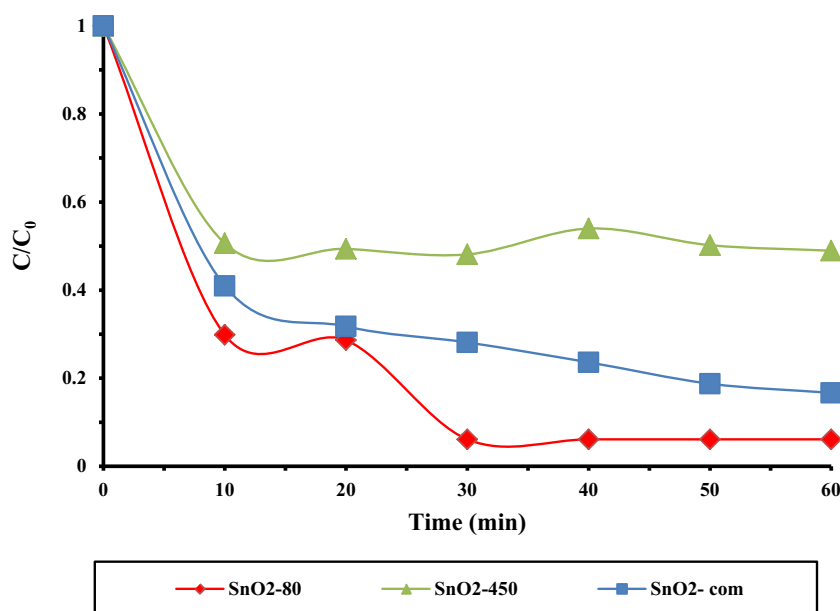
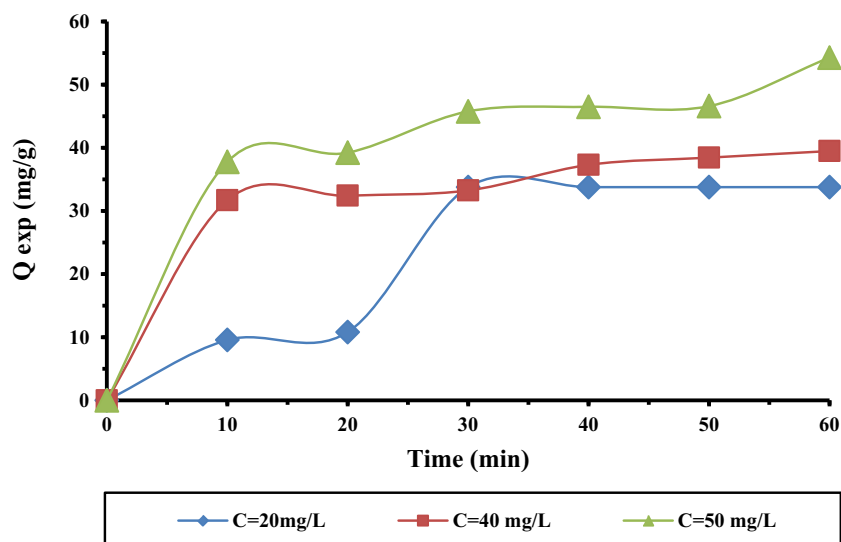


Fig. 8 Adsorption kinetic for CR adsorption onto SnO₂-80 nanoparticles at various initial concentration of the dye solution [(m/v) = 0.5 g/L, pH 7, T = 298 K and contact time of 60 min]



results (Fig. 8) indicated that the process is found to be very rapid initially, and the equilibrium is achieved within 60 min. As illustrated in Fig. 8, the adsorption efficiency of SnO₂-80 nanoparticles decreased from 84.41 % (33.766 mg/g) to 46.59 % (46.595 mg/g) when the initial concentration of dye was increased from 20 to 50 mg/L, respectively. Initial concentration provides an important driving force to overcome all mass transfer resistances of the dye between the aqueous and solid phases. Decrease in adsorption efficiency with initial concentration of dye is due to the dye agglomeration and the reduction of the thermal mobility of the adsorbed aggregates. Hence, a lower initial concentration of dye may enhance the process. So, for CR dye, the initial dye concentration of 20 mg/L is selected for subsequent experiments.

Effects of adsorbent dose

The effect of adsorbent dose of SnO₂-80 nanoparticles on the adsorption of CR dye is conducted over a range of adsorbent doses of 0.375 to 1 g/L. As elucidated in Fig. 9, the efficiency of CR adsorbed raised from 85.56 % (114.077 mg/g) to 93.77 % (93.766 mg/g) when the adsorbent dose increases from 0.375 to 0.5 g/L. This increase in adsorption efficiency with the adsorbent dose can be assigned to the increased surface area and the availability of more adsorption active sites. Further increase in the adsorbent dose beyond of 0.5 g/L, the adsorption efficiency gradually decreased, almost reaching 85.45 % (42.727 mg/g) at 1 g/L, due to overlapping of adsorption sites as a result of overcrowding of adsorbent. The maximum adsorbent dose of SnO₂-80 nanoparticles was found to be 0.5 g/L.

The adsorption kinetics of CR dye on SnO₂-80 nanoparticles at different initial concentration and

adsorbent doses, illustrated in Figs. 8 and 9, respectively, were treated with a pseudo-first-order and pseudo-second-order models, and the best fit model was selected according to the linear regression correlation coefficient, R² value. The pseudo-first-order model [29] is generally expressed as (Eq. (4)):

$$\log(Q_e - Q_t) = \log Q_e + \frac{K_1}{2303} t \quad (4)$$

where Q_e and Q_t (both in mg/g) are the amount of dye adsorbed per unit weight of adsorbent at equilibrium and at any time t , respectively. K_1 is pseudo-first order rate constant (min^{-1}). The adsorption rate constants (K_1) and the equilibrium adsorption capacity (Q_e), were calculated experimentally from the linear plots of $\log(Q_e - Q_t)$ versus t at different concentrations of CR (Fig. 10) and various adsorbent doses of SnO₂-80 (Fig. 12) are summarized in Tables 4 and 5, respectively.

The usual way to validate a model is to consider the goodness-of-fit using the linear regression coefficients, R^2 . However, using only the linear regression method may not be appropriate for comparing the goodness of fit of kinetic models. This is because an occurrence of the inherent bias resulting from linearization may affect the deduction. Therefore, in this study in addition to the linear regression analysis, the experimental data were tested with sum-of-square error (F_{error}) [30] to determine the best fitting kinetic model. The error function is given by (Eq. (5)):

$$F_{\text{error}} = \sqrt{\sum \frac{(Q_{e,\text{calc}} - Q_{e,\text{exp}})^2}{N}} \quad (5)$$

where $Q_{e,\text{exp}}$ is the experimentally determined sorption capacity; $Q_{e,\text{calc}}$ is the theoretical sorption capacity from the different kinetic models and N is the number of data points.



Fig. 9 Adsorption kinetic for CR adsorption onto SnO₂-80 nanoparticles at various adsorbent doses of SnO₂-80 sample [(CR) = 20 mg/L, pH 7, $T = 298$ K and contact time of 60 min]

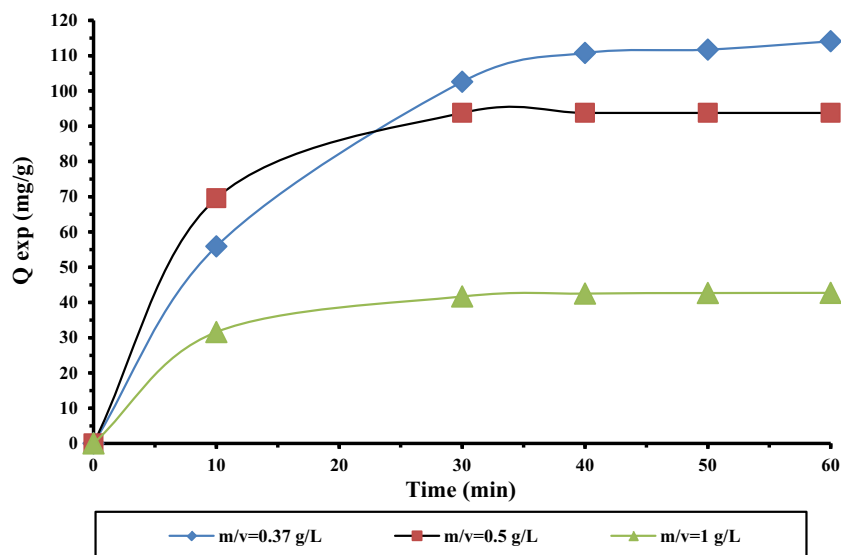


Fig. 10 Pseudo-first-order kinetic for CR adsorption onto SnO₂-80 nanoparticles at various initial concentration of the dye solution [(m/v) = 0.5 g/L, pH 7, $T = 298$ K and contact time of 60 min]

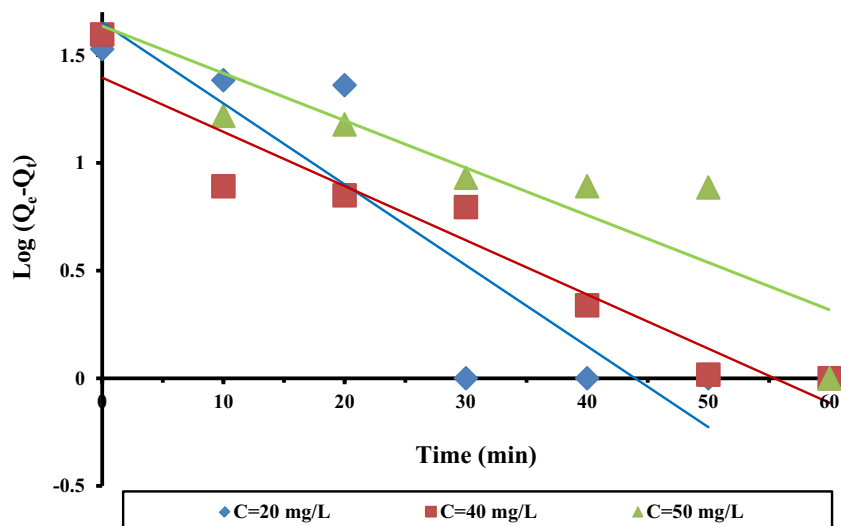


Table 4 Adsorption kinetic parameters for dyes adsorption onto SnO₂-80 nanoparticles at various initial concentration of the dye solution [(m/v) = 0.5 g/L, pH 7, $T = 298$ K and contact time of 60 min]

Experimental results		Pseudo-first-order kinetic model				Pseudo-second-order kinetic model			
C (mg/L)	$Q_{e,exp}$ (mg/g)	$Q_{e,calc}$ (mg/g)	K_1 (min ⁻¹)	R^2	F_{error}	$Q_{e,calc}$ (mg/g)	K_2 (g/mg.min)	R^2	F_{error}
20	33.766	44.864	0.086	0.81	11.09	33.784	0.287	1	0.01
40	39.479	24.912	0.058	0.92	13.27	40.161	0.008	0.99	0.34
50	46.595	43.291	0.050	0.82	13.32	47.847	0.002	0.99	0.53

The results show that the values of R^2 ranged from 0.81 to 0.92 for initial concentrations of CR of 20, 40, and 50 mg/L and from 0.81 to 0.99 for adsorbent doses of 0.37, 0.5 and 1 g/L, respectively. Furthermore, the experimental ($Q_{e,exp}$) data do not agree well with the calculated values ($Q_{e,cal.}$), as shown in Tables 4 and 5. The model is not able

to describe the experimental data properly because of the poor linear correlation and high F_{error} values (Tables 4, 5). All these observations show that the adsorption of CR onto SnO₂-80 does not follow first-order kinetics.

The pseudo-second-order model [31] is represented as (Eq. (6)):

Table 5 Adsorption kinetic parameters for dye adsorption onto SnO₂-80 nanoparticles at various adsorbent doses of SnO₂-80 sample [(CR) = 50 mg/L, pH 7, T = 298 K and contact time of 60 min]

Experimental results		Pseudo-first-order kinetic model				Pseudo-second-order kinetic model			
m/v (g/L)	Q _{e,exp} (mg/g)	Q _{e,calc} (mg/g)	K ₁ (min)	R ²	F _{error}	Q _{e,calc} (g/mg min)	K ₂ (min)	R ²	F _{error}
0.375	114.077	146.99	0.0838	0.96	32.91	123.46	0.00082	0.87	9.37
0.5	93.766	56.82	0.0696	0.81	37.74	96.154	0.00354	0.99	9.45
1	42.727	41.831	0.1324	0.99	37.74	43.86	0.0133	0.99	9.46

Fig. 11 Pseudo-second-order kinetic for CR adsorption onto SnO₂-80 nanoparticles at various initial concentration of the dye solution [(m/v) = 0.5 g/L, pH 7, T = 298 K and contact time of 60 min]

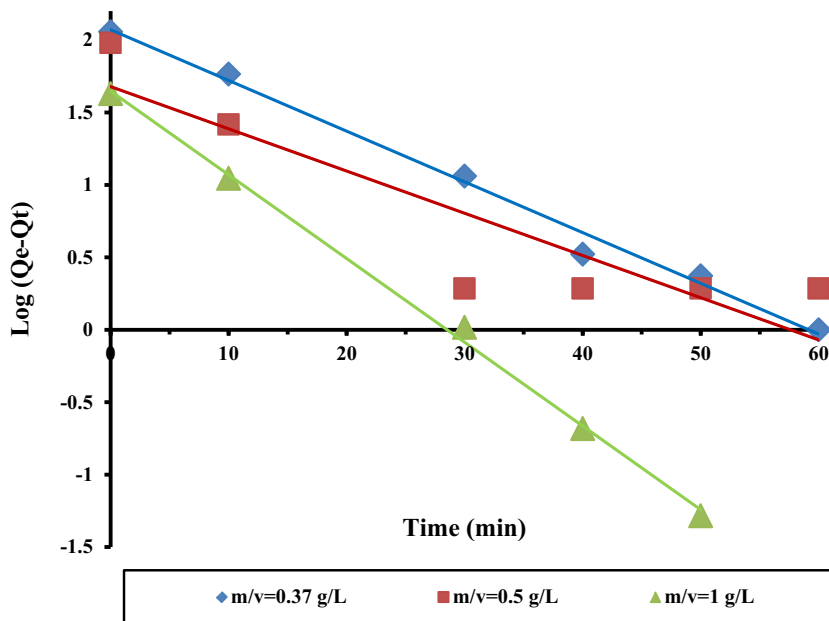
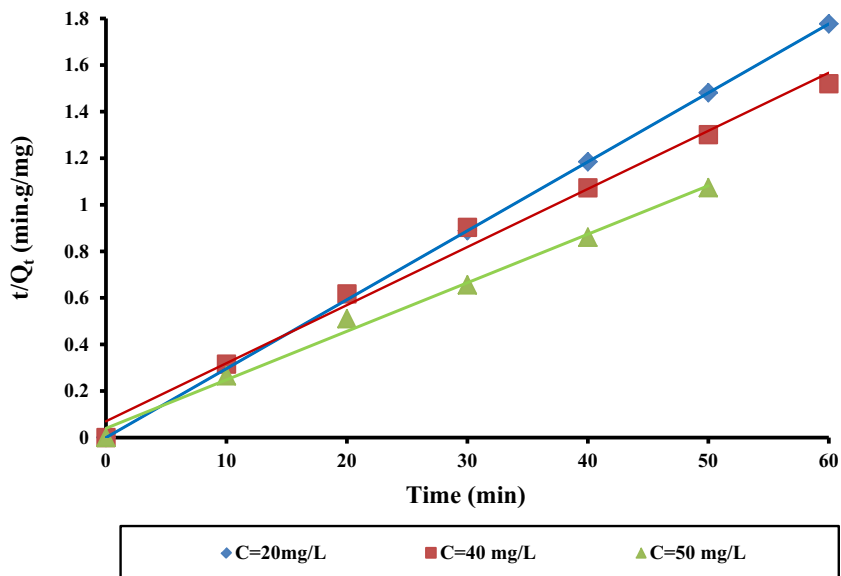


Fig. 12 Pseudo-first-order kinetic for CR adsorption at various adsorbent doses of SnO₂-80 nanoparticles [(CR) = 50 mg/L, pH 7, T = 298 K and contact time of 60 min]

Fig. 13 Pseudo-second-order kinetic for CR adsorption onto SnO₂-80 nanoparticles at various adsorbent doses of SnO₂-80 sample [(CR) = 50 mg/L, pH 7, T = 298 K and contact time of 60 min]

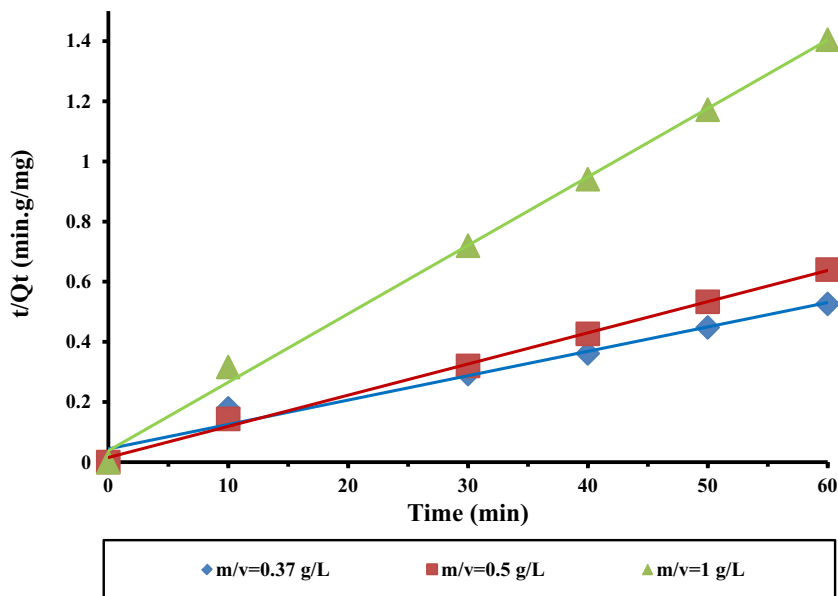


Fig. 14 Adsorption isotherm of dye adsorbed onto SnO₂-80 nanoparticles [(CR) = 20–50 mg/L, pH 7, T = 298 K and contact time of 60 min]

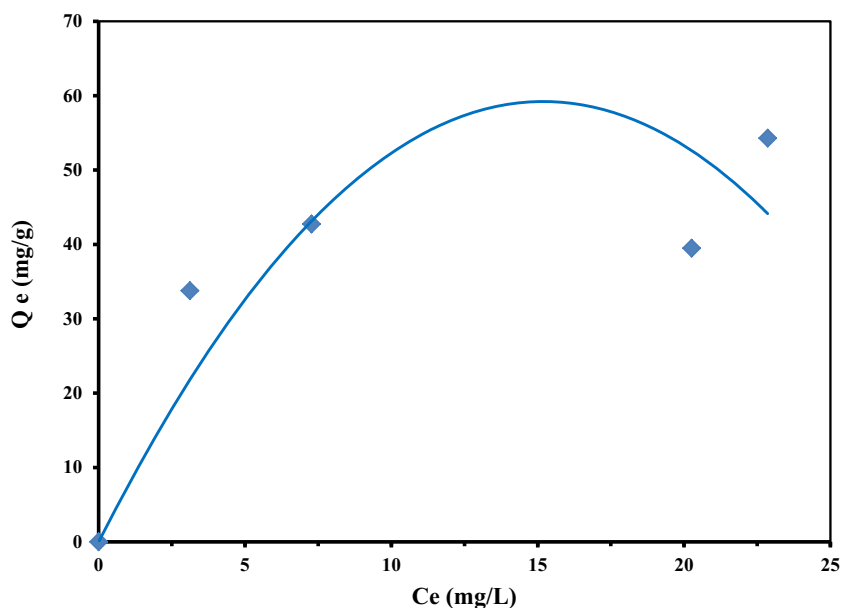


Table 6 Isotherm parameters of dye adsorbed onto SnO₂-80 nanoparticles for CR [(CR) = 50 mg/L, pH 7, T = 298 K and contact time of 60 min]

Isotherm	Temperature (298 K)	
Freundlich	K_F (L/g)	10.67
	$1/n$	0.94
	R^2	0.688
	F_{error} (%)	21.312
Langmuir	Q_{max} (mg/g)	48.309
	K_L (L/g)	1.178
	R_L	0.041–0.017
	R^2	0.939
	F_{error} (%)	0.2643

$$\frac{t}{Q_t} = \frac{1}{Q_e^2 K_2} + \frac{1}{Q_e} t \quad (6)$$

where K_2 is the pseudo-second-order constants (g/mg min). The initial adsorption rate, h (mg/g min⁻¹), as $t \rightarrow 0$ can be defined as (Eq. (7)):

$$h = K_2 Q_e^2 \quad (7)$$

The equilibrium adsorption capacity (Q_e), and the pseudo-second-order constant (K_2) can be determined experimentally from the slope and intercept of plots of t/Q_t versus t , respectively, at different concentrations of R (Fig. 11) and various adsorbent doses of SnO₂-80 (Fig. 13).



Fig. 15 Langmuir isotherm linearized model
 [(CR) = 20–50 mg/L, pH 7, $T = 298$ K and contact time of 60 min]

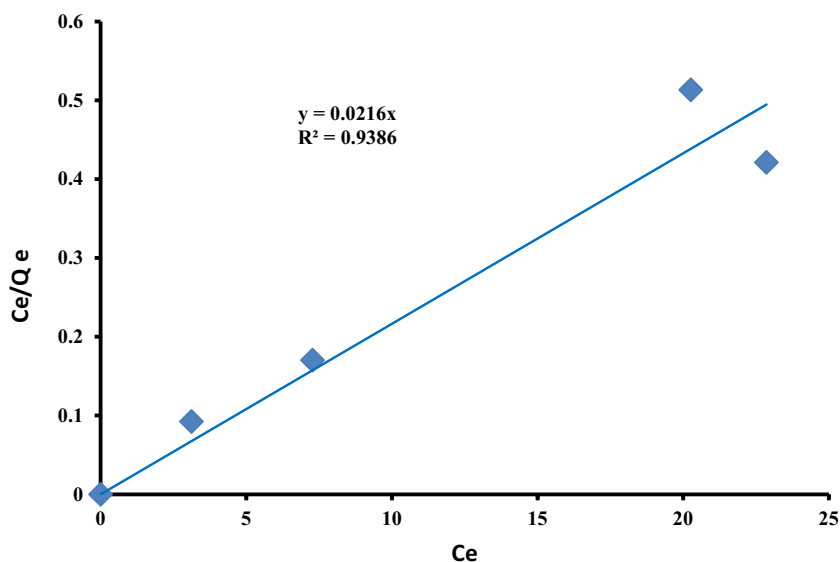
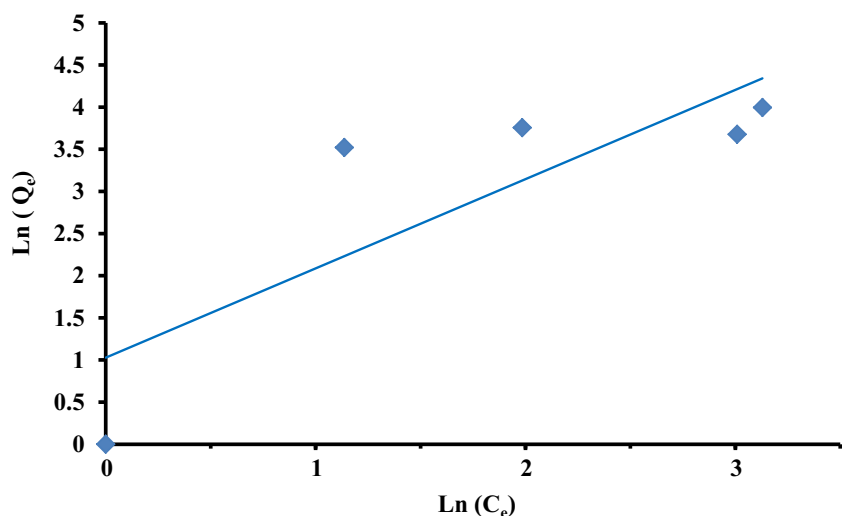


Fig. 16 Freundlich isotherm linearized model
 [(CR) = 20–50 mg/L, pH 7, $T = 298$ K and contact time of 60 min]



The R^2 values different CR dye concentrations and SnO₂-80 adsorbent doses of the linear portions are very high; and are close or equal to unity (0.99–1), which strongly suggests that adsorption of the CR follow the pseudo-second-order kinetic model wherein the overall rate of the adsorption process was controlled by chemisorptions which involved valency forces through electrons sharing between the adsorbent and adsorbate and higher adsorption energy. There is also a very good consistency between the calculated values ($Q_{e,cal.}$) and the experimental data ($Q_{e,exp}$) and the low values of its F_{error} values, as displayed in Tables 4 and 5.

Adsorption isotherm

To describe the adsorption behavior of Congo red dye by SnO₂-80 nanoparticle adsorbent, we have studied

adsorption isotherms. Inset in Fig. 14 shows equilibrium adsorption curves of CR on SnO₂-80 nanoparticles at room temperature. The adsorption of CR forms a typical Langmuir-type isotherm according to Giles classification system [32]. The adsorption capacity increased sharply at lower adsorption equilibrium dye concentration and thereafter the increase is gradual with an increase of equilibrium dye concentration. The maximum adsorption capacity of SnO₂-80 for CR was found to be 45.49 mg/g. Due to their widespread applications, the Langmuir [33] and Freundlich [34] isotherm models were applied to assess the performance of the adsorption process of CR dye onto SnO₂-80 nanoparticles.

To evaluate which model was best suited to describe these processes, and the error function (F_{error}) were analyzed; a lower result from the error function indicated a smaller difference between adsorption capacity calculated

Table 7 Comparison of Congo red adsorption capacities of various adsorbents

Types of adsorbent	Q_{\max} (mg/g)	References
Hydrogen peroxide treated tendu waste	134.4	[37]
Chitosan/montmorillonite nanocomposite	54.52	[38]
Metal hydroxides sludge	40	[39]
Hierarchical Ni(OH) ₂ nanosheets	82.9	[40]
Hierarchical NiO nanosheets	151.7	
Reagent NiO nanoparticles	39.7	
Ball-milled sugarcane bagasse	38.2	[41]
Magnetite nanoparticles	172.4	[42]
Fe ₂ O ₃ -SnO ₂ (Fe:Sn = 8:2) composite nanorod	182	[43]
CoFe ₂ O ₄ nanocrystals	244.5	[44]
Fe ₃ O ₄	149.7	
NiFe ₂ O ₄	97.1	
MnFe ₂ O ₄	92.4	
Chitosan-coated magnetic iron oxide	56.66	[45]
CTAB-modified kaolin (KC)	24.46	[46]
AuNPs-coated AC	71.05	[47]
AgNPs-coated AC	64.80	
Powdered eggshell	95.25	[48]
Chitosan hydrogel beads impregnated with CTAB	433.12	[49]
Surfactant-modified montmorillonite	351.0	[50]
<i>Alternanthera bettzickiana</i> plant powder	14.67	[51]
Activated carbon prepared from choir pith	6.72	[52]
Sugarcane bagasse	38.20	[41]
Mycelial pellets of <i>Trametes versicolor</i>	51.81	[53]
Soil (30 °C)	8.65	[54]
Organo-attapulgit	189.39	[55]
Burnt clay	22.86	[56]
Kaolin	5.44	[57]
Tamarind fruit shell	10.48	[58]
Water hyacinth roots	13.46	[59]
Carbon prepared from algae <i>Valoria bryopsis</i>	20.20	[60]
Chitosan hidrogel bead-SDS	186.02	[61]
Chitosan hydrogel beads impregnated with carbon nanotubes	450.40	[62]
Powdered eggshell	95.25	[63]
CoFe ₂ O ₄ magnetic nanoparticles	200.0-212.8	[64]
activated sulfidogenic sludge	238.90	[65]
γ -Fe ₂ O ₃ -TiO ₂	125	[66]
polyhedral Cu ₂ O nanoparticles	3904	[67]
Magnetic nanoparticles Mn-ferrites (MnFe ₂ O ₄).	41.99	[68]
Bis(triazole)-based 3D crystalline copper(II) MOF	656	[69]
Magnetic Ni _{0.5} Zn _{0.5} Fe ₂ O ₄ nanopowders	40.5	[70]
Mg(OH) ₂ hexagonal nanosheet-graphene oxide composites	118	[71]
α -Fe ₂ O ₃	253.8	[72]
Vaterite CaCO ₃	32.6	[73]
Hierarchical shell and hollow core structure gamma alumina (γ -Al ₂ O ₃)	835	[74]
SnO ₂ Derived from Sol-Gel method	48.31	Present work

by the model (Q_{calc}) and the experimental (Q_{exp}). F_{error} can be expressed according to Eq. (8) [35]:

$$F_{\text{error}} = \sum_{i=0}^P \left(\frac{Q_{i,\text{calc}} - Q_{i,\text{exp}}}{Q_{i,\text{exp}}} \right)^2 \quad (8)$$

where $Q_{i,\text{calc}}$ is a value of Q predicted by the fitted model; $Q_{i,\text{exp}}$ is a value of q measured experimentally; i indicates the values of the initial dye concentration of the experiments (20, 30, 40 and 50 mg/L); and P is the number of experiments performed.

The Freundlich isotherm is an empiric equation employed to describe heterogenous systems. The logarithmic form of the Freundlich equation Eq. (9) is:

$$\text{Ln}Q_e = \text{Ln}K_F + \frac{1}{n} \text{Ln}C_e \quad (9)$$

where K_F and $1/n$ are Freundlich adsorption isotherm constants (L/mg), being indicative of the extent of the adsorption and the degree of nonlinearity between solution concentration and adsorption [the adsorption process to be linear ($n = 1$), chemical ($n < 1$) and favorable physical process ($n > 1$)], respectively. Therefore K_F and $1/n$ were calculated from the plots of $\text{Ln}Q_e$ against $\text{Ln}C_e$. These values, along with r and F_{error} , are shown in Table 6.

The Langmuir adsorption isotherm assumes that adsorption takes place at specific homogeneous sites within the adsorbent and has found successful application in many adsorption processes of monolayer adsorption. The linear form of the Langmuir isotherm equation is represented by the following equation Eq. (10):

$$\frac{C_e}{Q_e} = \frac{1}{K_L Q_{\text{max}}} + \frac{C_e}{Q_{\text{max}}} \quad (10)$$

where Q_{max} (mg/g) is the maximum amount of the dye per unit weight of SnO_2 -80 nanoparticles to form a complete monolayer coverage on the surface bound at high equilibrium dye concentration C_e (mg/L) and K_L (L/g) is the Langmuir constant related to the affinity of binding sites. A plot of C_e/Q_e versus C_e leads to a straight line with the slope of $1/Q_{\text{max}}$ and an intercept of $1/Q_{\text{max}} K_L$.

The essential characteristics of Langmuir isotherm can be expressed by a dimensionless constant called equilibrium parameter R_L that is defined by the following equation Eq. (11):

$$R_L = \frac{1}{(1 - K_L C_0)} \quad (11)$$

where K_L and C_0 are the same as defined before. The value of R_L calculated from the above expression. The nature of the adsorption process to be either unfavorable ($R_L > 1$), linear ($R_L = 1$), favourable ($0 < R_L < 1$) or irreversible ($R_L = 0$).

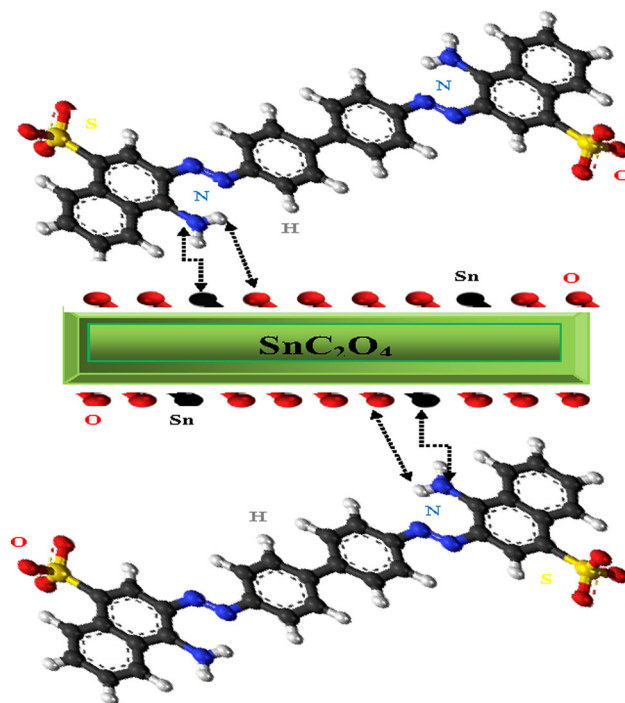


Fig. 17 Schematic illustration of CR dye removal process

Figures 15 and 16, show the plot of the experimental data based on Langmuir and Freundlich isotherm models, respectively. Table 2 depicts the calculated values of Langmuir and Freundlich model's parameters. Based on the regression coefficients (R^2) of the linearized form of both equations and their errors function (F_{error}), the Langmuir model yields a better fit for the experimental equilibrium adsorption data than the Freundlich model. The high fit to the Langmuir model suggests that the adsorption is limited with monolayer coverage. All the R_L -values for the adsorption of CR onto SnO_2 -80 nanoparticles are in the range of 0–1, suggesting that the adsorption is favorable under the conditions proposed by the Langmuir model. The R^2 value is greater than 0.93, its F_{error} is lower than 0.27, thus, lower than the one obtained for the Freundlich model. The maximum adsorption capacity of SnO_2 -80 nanoparticles for CR calculated from the Langmuir isotherm model was 48.31 mg/g. Thus, these data suggest that Langmuir isotherm model was suitably fitted [36].

According to Langmuir isotherm model, the maximum adsorption capacity (O_{exp}) for the adsorption of CR on SnO_2 is found to be 48.31 mg/g. The maximum adsorption capacity (O_{max}) for the adsorption of CR on SnO_2 nanoparticles compared to other adsorbents is listed in Table 7. It can be seen that adsorption capacity varies and depends on the properties of the individual adsorbent, the extent of surface/surface modification, the initial concentration of the adsorbate, range of molecular size fraction of

adsorbate and degree of ionization per unit weight of adsorbate. It is observed also that the prepared SnO₂-80 nanoparticles are an efficient adsorbent for adsorption of Congo red from aqueous solution.

Discussion of mechanism

The surface chemistry of the adsorbents plays a major role in the adsorption. The particles of SnC₂O₄ are roughly in elongated prisms shape with average particle size of 10 μm. The oxygen content of the surface is about 80 % giving a O (at%)/Sn (at%) ration of approximately 4:1, the stoichiometry of SnC₂O₄. The large number and array of different functional groups on the SnC₂O₄ surfaces (e.g., oxygenic and carbonyl) implied the existence of many types of adsorbent–solute interaction. As shown in Fig. 17, the adsorption of the azo dye on SnC₂O₄ layer is favored, mainly due to the electrostatic interaction between the Sn²⁺ center and the electron rich nitrogen atoms of CR moiety [75]. Additionally, SnC₂O₄ nanoparticles can capture more dye molecules via the formation of hydrogen bond [68].

Conclusion

In Summary, the nanoparticles SnO₂ have been successfully synthesized via a sol-gel method. The as-prepared SnO₂ was characterized using a number of techniques such as thermogravimetric analysis coupled with mass spectroscopy (TG-SM), X-ray diffraction (XRD) and scanning electron microscope (SEM). Batch experiments were carried out to study the adsorption kinetics of Congo red azo dye, as probe pollutant, on SnO₂. The effect of varying parameters such as contact time, initial dye concentration and adsorbent dose on the adsorption process was investigated. The results showed that the SnO₂ catalysts have high crystallinity with tetragonal rutile structure and average particle size about 13–23 nm. The untreated sample SnO₂-80 exhibited high efficiency (84.41 %) after 60 min of exposure time, which was 2 times as much as that of SnO₂-450 sample. Experimental kinetic data were satisfactory correlated with the pseudo-second-order kinetic model, with highest correlation coefficients ($R^2 \geq 0.99$). The formation of hydrogen bond and the electrostatic interaction between the Sn²⁺ center and the electron rich nitrogen atoms of CR moiety were believed to be was the main adsorption mechanism. Regarding the adsorption equilibrium, the experimental results suggest that the Langmuir model was applicable. The obtained SnO₂ is a promising candidate for potential application in organic pollutant uptake from contaminated water sources.

Acknowledgments The authors would like to acknowledge University of Science and Technology Mohammed Boudiaf, Oran, Algeria, the University Dr. Moulay Tahar, Saida, Algeria and Unit of Catalysis and Solid State Chemistry of Lille 1 University, Lille, France for providing the facilities to carry out this research work.

Open Access This article is distributed under the terms of the Creative Commons Attribution 4.0 International License (<http://creativecommons.org/licenses/by/4.0/>), which permits unrestricted use, distribution, and reproduction in any medium, provided you give appropriate credit to the original author(s) and the source, provide a link to the Creative Commons license, and indicate if changes were made.

References

- Liu H, Hu C, Wang Z (2006) Composite-hydroxide-mediated approach for the synthesis of nanostructures of complex functional-oxides. *Nano Lett* 6:1535–1540
- Derbal A, Omeiri S, Bouguelia A, Trari M (2008) Characterization of new heterosystem CuFeO₂/SnO₂ application to visible-light induced hydrogen evolution. *Int J Hydrogen Energy* 33:4274–4282
- Wang Y, Jiang X, Xia YJ (2003) A solution-phase, precursor route to polycrystalline SnO₂ nanowires that can be used for gas sensing under ambient conditions. *J Am Chem Soc* 125:16176–16177
- Snaith HJ, Ducati C (2010) SnO₂-based dye-sensitized hybrid solar cells exhibiting near unity absorbed photon-to-electron conversion efficiency. *Nano Lett* 10:1259–1265
- Li LJ, Zong FJ, Cui XD, Ma HL, Wu XH, Zhang QD, Wang YL, Yang F, Zhao JZ (2007) Structure and field emission properties of SnO₂ nanowires. *Mater Lett* 61:4152–4155
- Zhou W, Liu R, Wan Q, Zhang Q, Pan A, Guo L, Zou B (2009) Bound exciton and optical properties of SnO₂ one-dimensional nanostructures. *J Phys Chem C* 113:1719–1726
- Yang H, Ouyang J, Tang A, Xiao Y, Li X, Dong X (2006) Electrochemical synthesis and photocatalytic property of cuprous oxide nanoparticles. *Mater Res Bull* 41:1310–1318
- Zhang L, Li J, Chen Z, Tang Y, Yu Y (2006) Preparation of Fenton reagent with H₂O₂ generated by solar light-illuminated nano-Cu₂O/MWNTs composites. *Appl Catal A* 299:292–297
- Wang Q-Q, Lin B-Z, Xu B-H, Li XL, Chen ZJ, Pian XT (2010) Preparation and photocatalytic properties of mesoporous SnO₂-hexaniobate layered nanocomposite. *Microporous Mesoporous Mater* 130:344–351
- Wang GX, Chen Y, Yang L, Yao J, Needham S, Liu HK, Ahn JH (2005) Synthesis of nanocrystalline transition metal and oxides for lithium storage. *J Power Sources* 146:487–491
- Li WJ, Shi EW, Fukuda T (2003) Particle size of powders under hydrothermal conditions. *Cryst Res Tech* 38:847–858
- Fraigi LB, Lamas DG, Walsoe de Reça NE (2001) Comparison between two combustion routes for the synthesis of nanocrystalline SnO₂ powders. *Mater Lett* 47:262–266
- Sangami G, Dharmaraj N (2012) UV-visible spectroscopic estimation of photodegradation of rhodamine-B dye using tin(IV) oxide nanoparticles. *Spectr Chim Acta Part A Mol Biomol Spect* 97:847–852
- Talebian N, Zavvare HSH (2014) Enhanced bactericidal action of SnO₂ nanostructures having different morphologies under visible light: influence of surfactant. *J Photochem Photobiol B Biol* 130:132–139
- Song KC, Kang Y (2000) Preparation of high surface area tin oxide powders by a homogeneous precipitation method. *Mater Lett* 42:283–289

16. Santos OD, Weiler ML, Junior DQ, Medina AN (2001) CO gas-sensing characteristics of SnO₂ ceramics obtained by chemical precipitation and freeze-drying. *Sens Act B* 75:83–87
17. Iburguen CA, Mosquera A, Parra R, Castro MS, Rodriguez-Paez JE (2007) Synthesis of SnO₂ nanoparticles through controlled precipitation route. *Mater Chem Phys* 101:433–440
18. Boreddy R (2011) Advances in nanocomposites, synthesis, characterization and industrial applications < chapter 14 Dep. Materials and Production Engineering, University “Federico II” of Naples, Italy, pp 323–340
19. Kaliszewski MS, Heuer AH (1990) Alcohol interaction with zirconia powders. *J Amer Ceram Soc* 73:1504–1509
20. Azaroff LV (1968) Elements of X-ray crystallography. McGraw-Hill, New York, pp 331–568
21. Pullar RC, Taylor MD, Bhattacharya AK (1988) The manufacture of yttrium aluminium garnet (YAG) fibres by blow spinning from a sol-gel precursor. *J Eur Cer Soc* 18:1759–1764
22. Cullity BD (1956) Elements of X-ray diffraction. Addison-Wesley Publishing Co., New York, pp 98–99
23. Hu C, Zhang Z, Liu H, Gao P, Lin Wang Z (2006) Direct synthesis and structure characterization of ultrafine CeO₂ nanoparticles. *Nanotechnology* 17:5983–5987
24. Taib H, Sorrell CC (2007) Preparation of tin oxide. *J Aust Ceram Soc* 43:56–61
25. He SB, Wang SF, Ding QP, Yuan XD, Zheng WG, Xiang X, Li ZJ, Zu XT (2013) Role of chelating agent in chemical and fluorescent properties of SnO₂ nanoparticles. *Chin Phys B* 22:058102
26. Rejani P, Radhakrishnan A, Beena B (2014) Adsorption of Pb(II) on nano sized SnO₂ derived from Sol-Gel method. *Int J Chem Eng Appl* 5:244–248
27. Sun ZX, Lou G, Liu X, Li H, Su Z (2005) A new method for preparing V₂O₃ nanopowder. *Mater Lett* 59:2729–2731
28. Amel Khalfaoui, Bendjamaa I, Bensid T, Hassen MA, Derbal K (2014) Effect of calcination on orange peels characteristics: application of an industrial dye adsorption. *Chem Eng Trans* 38:361–366
29. Lagergen S (1898) Zur theorie der sogenannten adsorption gelster stoffe, *Kungliga Svenska Vetenskapsakademiens. Handlingar* 24:1–39
30. Wang XS, Li Z, Tao SR (2009) Removal of chromium (VI) from aqueous solution using walnut hull. *J Environ Manag* 90:721–729
31. Ho YS, McKay GA (1999) *Resour Conserv Recycl* 25:171–193
32. Giles CH, Mac Ewan TH, Nakhwa SN, Smith D (1960) Studies in adsorption. Part XI. A system of classification of solution adsorption isotherms, and its use in diagnosis of adsorption mechanisms and in measurement of specific surface areas of Solids. *J Chem Soc*:3973–3993
33. Langmuir I (1916) The constitution and fundamental properties of solids and liquids. *J Am Chem Soc* 38(2221–2295):1916
34. Freundlich H, Umber MF (1906) Die Adsorption in lasugen. *Z Phys Chem* 57:385–470
35. Lima ECB, Royer JCP, Vaghetti JL, Brasil NM, Simon AA, dos Santos Jr FA, Pavan SLP, Dias EV, Benvenuto Silva EA (2007) Adsorption of Cu(II) on *Araucaria angustifolia* wastes: determination of the optimal conditions by statistic design of experiments. *J Hazard Mater* 140:211–220
36. Yang S, Wu Z, Huang LP, Zhou B, Lei M, Sun L, Tian Q, Pan J, Wu W, Zhang H (2014) Significantly enhanced dye removal performance of hollow tin oxide nanoparticles via carbon coating in dark environment and study of its mechanism. *Nanoscale Res Lett* 9:442–451
37. Sharma J, Janveja B (2008) A study on removal of congo red dye from the effluents of textile industry using rice husk carbon activated by steam. *Rasayan J Chem* 4:936–942
38. Wang L, Wang A (2007) Adsorption characteristics of Congo red onto the chitosan/montmorillonite nanocomposite. *J Hazard Mater* 147:979–985
39. Attallah MF, Ahmed IM, Hamed MM (2013) Treatment of industrial wastewater containing Congo red and naphthol green B using low-cost adsorbent. *Environ Sci Pollut Res Int* 20:1106–1116
40. Cheng B, Le Y, Cai W, Yu J (2011) Synthesis of hierarchical Ni(OH)₂ and NiO nanosheets and their adsorption kinetics and isotherms to Congo red in water. *J Hazard Mater* 185:889–897
41. Zhang Z, Moghaddam L, O’Hara IM, Doherty WOS (2011) Congo red adsorption by ball-milled sugarcane bagasse. *Chem Eng J* 178:122–128
42. Giri SK, Das NN, Pradhan GC (2011) Synthesis and characterization of magnetite nanoparticles using waste iron ore tailings for adsorptive removal of dyes from aqueous solution. *Colloids Surf A* 389:43–49
43. Jyoti PD, Braja GM, Garudadhvaj H (2014) Fe₂O₃-SnO₂ composite nanorods: facile synthesis and sorption properties. *J Environ Chem Eng* 2:2188–2198
44. Wang L, Li J, Wang Y, Zhao L, Jiang Q (2011) Adsorption capability for Congo red on nanocrystalline MFe₂O₄ (M = Mn, Fe, Co, Ni) spinel ferrites. *Chem Eng J*. doi:10.1016/j.cej.2011.10.088
45. Zhu H, Zhang M, Liu Y, Zhang L, Han R (2012) Study of congo red adsorption onto chitosan coated magnetic iron oxide in batch mode. *Desalination Wat Treat* 37:46–54
46. Zenasni MA, Meroufel B, Merlin A, George B (2014) Adsorption of Congo red from aqueous solution using CTAB-Kaolin from bechar Algeria. *J Surf Eng Mat Adv Technol* 4:332–341
47. Pal J, Deb MK (2014) Efficient adsorption of congo red dye from aqueous solution using green synthesized coinage nanoparticles coated activated carbon beads. *Appl Nanosci* 4:967–978
48. Zulfikar MA, Setiyanto H (2013) Adsorption of Congo red from aqueous solution using powdered egg shell. *Inter J Chem Tech Res* 5:1532–1540
49. Chatterjee S, Lee DS, Lee MW, Woo SH (2009) Enhance adsorption of congo red from aqueous solutions by chitosan hydrogel beads impregnated with cetyl trimethyl ammonium bromide. *Bioresour Technol* 100:2803–2809
50. Wang L, Wang A (2008) Adsorption properties of Congo Red from aqueous solution onto surfactant modified montmorillonite. *J Hazard Mater* 160:173–180
51. Patil AK, Shrivastava VS (2010) *Alternanthera bettzichiana* plant powder as low cost adsorbent for removal of Congo red from aqueous solution. *Inter J Chem Tech Res* 2:842–850
52. Namasivayam C, Kavitha D (2002) Removal of Congo Red from water by adsorption onto activated carbon prepared from choir pith, an agricultural solid waste. *Dyes Pigment* 54:47–58
53. Binupriya AR, Sathishkumar M, Swaminathan K, Ku CS, Yun SE (2008) Comparative studies of removal of Congo red by native and modified mycelial pellets of *Trametes versicolor* in various reactor modes. *Bioresour Technol* 99:1080–1088
54. Smaranda C, Gavrilesco M, Bulgariu D (2011) Studies on sorption of Congo red from aqueous solution onto soil. *Inter J Environ Res* 5:177–188
55. Chen H, Zhao J (2009) Adsorption study for removal of Congo red anionic dye using organo-attapulgite. *Adsorption* 15:381–389
56. Mumin MA, Khan MMR, Akhter KF, Uddin MJ (2007) Potentially of open burnt clay as an adsorbent for the removal of Congo red from aqueous solution. *Inter J Environ Sci Technol* 4:525–532
57. Vimonses V, Lei S, Jin B, Chow CWK, Saint C (2009) Kinetic study and equilibrium isotherm analysis of Congo Red adsorption by clay minerals. *Chem Eng J* 148:354–364
58. Reddy MCS (2006) Removal of direct dye from aqueous solutions with an adsorbent made from tamarind fruit shell, an agricultural solid waste. *J Sci Indus Res* 65:443–446
59. Rajamohan N (2009) Equilibrium studies on sorption of an anionic dye onto acid activated water hyacinth roots. *Afr J Environ Sci Technol* 3:399–404



60. Jayaraj R, Thanaraj PJ, Natarajan ST, Prasath PMD (2011) Removal of Congo red dye from aqueous solution using acid activated eco-friendly low cost carbon prepared from marine algae *Valoria bryopsis*. *J Chem Pharm Res* 3:389–396
61. Chatterjee S, Chatterjee T, Woo SH (2011) Adsorption of Congo Red from aqueous solution using chitosan hydrogel beads formed by various anionic surfactants. *Separ Sci Technol* 46:986–996
62. Chatterjee S, Lee MW, Woo SH (2010) Adsorption of congo red by chitosan hydrogel beads impregnated with carbon nanotubes. *Bioresour Technol* 101:1800–1806
63. Yeddou N, Bensmaili A (2007) Equilibrium and kinetic modelling of iron adsorption by eggshells in a batch system: effect of temperature. *Desalination* 206:127–134
64. Ghaemi M, Absalan G, Sheikhan L (2014) Adsorption characteristics of Titan yellow and Congo red on CoFe_2O_4 magnetic nanoparticles. *J Iran Chem Soc* 11:1759–1766
65. Rasool K, Lee DS (2015) Characteristics, kinetics and thermodynamics of Congo Red biosorption by activated sulfidogenic sludge from an aqueous solution. *Int J Environ Sci Technol* 12:571–580
66. Yu M, Zhao S, Wu H, Asuha S (2013) Efficient removal of Congo red by magnetically separable mesoporous TiO_2 modified with $\gamma\text{-Fe}_2\text{O}_3$. *J Porous Mater* 20(20):1353–1360
67. Shu Jinxia, Wang Z, Huang Y, Huang N, Ren C, Zhang W (2015) Adsorption removal of Congo red from aqueous solution by polyhedral Cu_2O nanoparticles: kinetics, isotherms, thermodynamics and mechanism analysis. *J Alloys Compounds* 633:338–346
68. Liu X, Zhang Z, Shi W, Zhang Y, An S, Zhang L (2015) Adsorbing properties of magnetic nanoparticles Mn-ferrites on removal of Congo Red from aqueous solution. *J Disper Sci Technol* 36:462–470
69. Wang XX, Li ZX, Yuc B, Hecke KV, Cui GH (2015) Synthesis and characterizations of a bis(triazole)-based 3D crystalline copper(II) MOF with high adsorption capacity for congo red dye inorganic. *Chem Commun* 54:9–11
70. Liu R, Fu H, Yin H, Wang P, Lu L, Tao Y (2015) A facile sol combustion and calcination process for the preparation of magnetic $\text{Ni}_{0.5}\text{Zn}_{0.5}\text{Fe}_2\text{O}_4$ nanopowders and their adsorption behaviors of Congo red. *Powder Technol* 274:418–425
71. Liu M, Ja Xu, Cheng B, Ho W, Yu J (2015) Synthesis and adsorption performance of $\text{Mg}(\text{OH})_2$ hexagonal nanosheet–graphene oxide composites. *Appl Surf Sci* 332:121–129
72. Hao T, Yang C, Rao X, Wang J, Niu C, Su X (2014) Facile additive-free synthesis of iron oxide nanoparticles for efficient adsorptive removal of Congo red and Cr(VI). *Appl Surf Sci* 292:174–180
73. Kai YC, Chin HC, Sarani Z, Mohd SS (2014) Vaterite calcium carbonate for the adsorption of Congo red from aqueous solutions. *J Environ Chem Eng* 2:2156–2161
74. Lan S, Guo N, Liu L, Wu X, Li L, Gan S (2013) Facile preparation of hierarchical hollow structure gamma alumina and a study of its adsorption capacity. *Appl Surf Sci* 283:1032–1040
75. Sangami G, Dharmaraj N (2012) UV–visible spectroscopic estimation of photodegradation of rhodamine-B dye using tin (IV) oxide nanoparticles. *Spectrochim Acta Part A: Mol Biomol Spectrosc* 97:847–852

